ACS NANO

www.acsnano.org

Nanometer-Scale Heterogeneous Interfacial Sapphire Wafer Bonding for Enabling Plasmonic-Enhanced Nanofluidic Mid-Infrared Spectroscopy

Jikai Xu,‖ Zhihao Ren,‖ Bowei Dong, Xinmiao Liu, Chenxi Wang,* Yanhong Tian,* and Chengkuo Lee*

Cite This: *ACS Nano* 2020, 14, 12159−12172

Read Online

ACCESS | Metrics & More | Article Recommendations | Supporting Information

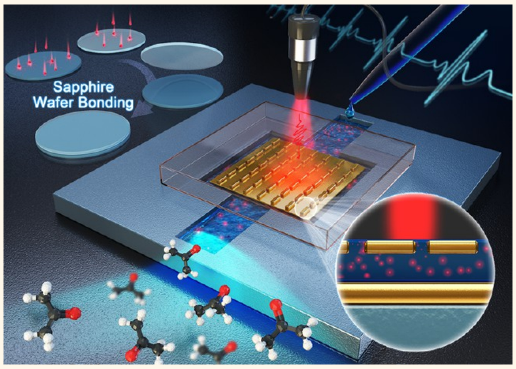

ABSTRACT: As one of the most effective surface-enhanced infrared absorption (SEIRA) techniques, metal−insulator−metal structured metamaterial perfect absorbers possess an ultrahigh sensitivity and selectivity in molecular infrared fingerprint detection. However, most of the localized electromagnetic fields (*i.e.*, hotspots) are confined in the dielectric layer, hindering the interaction between analytes and hotspots. By replacing the dielectric layer with the nanofluidic channel, we develop a sapphire (Al_2O_3)-based mid-infrared (MIR) hybrid nanofluidic-SEIRA (HN-SEIRA) platform for liquid sensors with the aid of a low-temperature interfacial heterogeneous sapphire wafer direct bonding technique. The robust atomic bonding interface is confirmed by transmission electron microscope observation. We also establish a design methodology for the HN-SEIRA sensor using coupled-mode theory to carry out the loss engineering and experimentally validate its feasibility through the accurate nanogap control. Thanks to the capillary force, liquid analytes can be driven into sensing hotspots without external actuation systems. Besides, we demonstrate an *in situ* real-time dynamic monitoring process for the acetone molecular diffusion in deionized water. A small concentration change of 0.29% is distinguished and an ultrahigh sensitivity (0.8364 pmol^{-1} %) is achieved. With the aid of IR fingerprint absorption, our HN-SEIRA platform brings the selectivity of liquid molecules with similar refractive indexes. It also resolves water absorption issues in traditional IR liquid sensors thanks to the sub-nm long light path. Considering the wide transparency window of Al_2O_3 in MIR (up to 5.2 μm), the HN-SEIRA platform covers more IR absorption range for liquid sensing compared to fused glass commonly used in micro/nanofluidics. Leveraging the aforementioned advantages, our work provides insights into developing a MIR real-time liquid sensing platform with intrinsic IR fingerprint selectivity, label-free ultrahigh sensitivity, and ultralow analyte volume, demonstrating a way toward quantitative molecule identification and dynamic analysis for the chemical and biological reaction processes.

KEYWORDS: *surface-enhanced infrared absorption, mid-infrared dynamic monitoring, plasmonics, nanofluidic, wafer direct bonding*

With the booming of the Internet of Things (IoT), sensing technologies for liquids, biomolecules, and gases have become more and more critical in the field of personal healthcare and environmental monitoring.[1] Mid-infrared (MIR) spectroscopy provides a powerful tool to identify and characterize analytes with real-time, label-free, and non-invasive fashion. However, due to the inherently weak light−matter interaction,[2−6] IR spectroscopy suffers from a bulky device size, low sensitivity, and poor resolution, which limit its practical applications. To improve the detection sensitivity, metamaterial perfect absorbers (MPAs) with engineered periodic plasmonic nanoantenna array structures become preferred candidates for miniaturized surface-enhanced IR absorption (SEIRA) spectroscopy.[7−10] When the IR radiation acts on the MPAs, the enhanced electromagnetic field (*i.e.*, hotspots) will be excited in the cavities and among the adjacent metal objects.[11−14] Meanwhile, due to the near-field plasmon-phonon coupling, the enhanced absorption

Received: July 12, 2020
Accepted: August 19, 2020
Published: August 19, 2020

https://dx.doi.org/10.1021/acsnano.0c05794

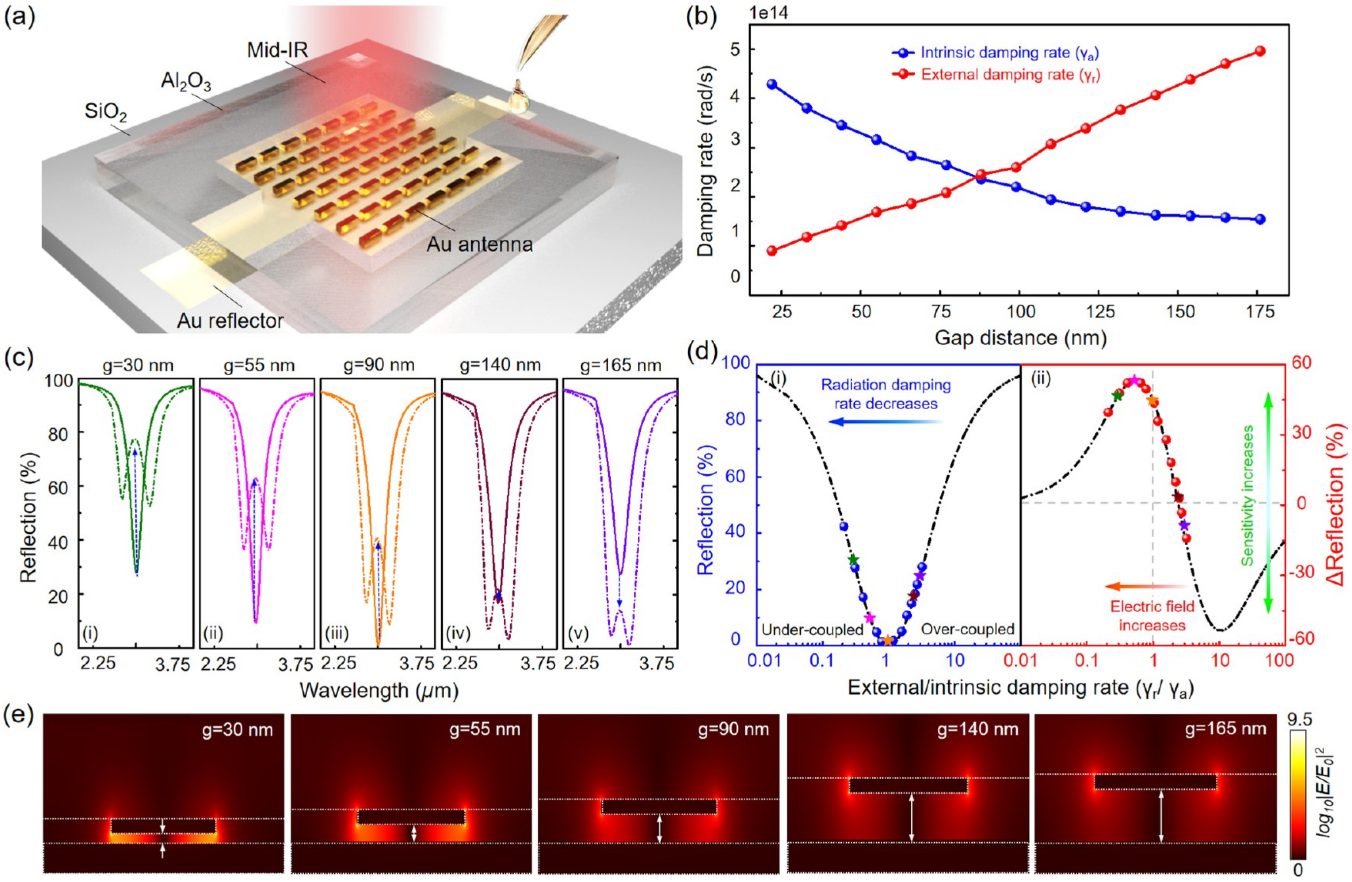

Figure 1. Concept of the self-driven 3D plasmonic Al_2O_3-based MIR sensing platform and simulation results for the theoretical support of the signal enhancement. (a) Device configuration of the 3D plasmonic liquid sensor in MIR. (b) Tuning of the external (γ_r) and intrinsic (γ_a) losses at varied gap distances. Both γ_r and γ_a are extracted from the FDTD simulation results in Figure S2. (c) Simulated reflected spectra with and without DI water at typical nanogaps. (d) Fitting results between our proposed theoretical curves and simulation data. (e) Simulated electrical field distribution corresponding to the nanogaps in (c). The color scale is common to all five panels.

signals can be detected when the molecules are spatially overlapped with the nanoscale hotspot regions. Currently, metal−insulator−metal (MIM)-based MPAs rely on the interaction of molecules near the top surface of plasmonic structures.[15−21] However, this kind of detection only utilizes small parts of the enhanced electromagnetic field that originate from the top metasurface, hindering the coupling between molecules and hotspots. Therefore, the detection sensitivity is restricted by the inefficient usage of hotspots.

To overcome this bottleneck, the concept of hybrid plasmonics-nanofluidic has been proposed and demonstrated to be effective.[22] This hybrid device integrates the MPA into the nanofluidics. Leveraging the nanofluidic technology, analytes can be accurately delivered to hotspot regions through the nano/microchannels. With engineered plasmonic structures, the hybrid device also performs a quadrupole resonance mode, which can be lithographically tuned by the length of the nanoantennas. However, it is still a challenge to precisely control the nanometer-scale gap in hybrid plasmonics-nanofluidics because of the complex fabrication process. Therefore, it leaves a technology barrier to improve further the sensing performance, which is highly dependent on the fluidic thickness. Additionally, there are no theoretical studies or experimental research reported to provide a systematic methodology to design this kind of hybrid device. Considering damping losses and resonance modes can be tuned by the thickness of the dielectric in the MIM system,[23−27] we can utilize the direct bonding technique to fabricate the nanogaps to study the coupling conditions of the system. To realize the device configuration, direct bonding becomes a crucial process to ensure the device sealing and control the losses tuning by precisely adjusted nanogaps. Although soft materials (*e.g.*, PDMS, PMMA, PS, *etc.*) have excellent bonding abilities with different rigid materials,[28−30] they are not suitable for the nanochannel/chamber fabrication because of the collapse.[31,32] So far, fabrication of the nanofluidic device mainly uses fused silica (SiO_2) because of its mature low-temperature bonding technique, such as O_2/CF_4 plasma activation,[33] sequential plasma activation,[34] and VUV/O_3 activation.[35,36] In the sensing applications, MIR beyond 3 μm is a vital wavelength range that covers the fingerprint of gas and biological molecules, such as N−H,[37] O−H,[38] C−H,[39] C═O,[40] *etc.* Unfortunately, SiO_2 only has a high transmittance of <2.8 μm wavelength. Consequently, SiO_2-based devices limit their applications. Many transparent infrared materials (*e.g.*, CaF_2[2,41−43] and MgF_2[44]) have been used as the substrates of metasurfaces. Few studies have focused on the integration of transparent infrared materials and other materials to create three-dimensional (3D) plasmonic cavities for ultrasensitive detection. Although UV-activated CaF_2/SiO_2 bonding has been reported, the bonding strength and interface were still not strong enough to resist the water stress corrosion for a continuous long-time dynamic sensing.[22] Therefore, the development of bonding techniques for transparent IR materials is essential for expanding the detection categories and increasing the sensitivity in 3D plasmonic sensing applications.

In this paper, we demonstrated a self-driven sapphire (Al_2O_3)-based hybrid nanofluidic-SEIRA (HN-SEIRA) sensing platform with ultrahigh sensitivity. To fabricate the robust quasi-3D structures, we developed a plasma-activated method for low-temperature direct bonding of Al_2O_3 and SiO_2. Direct bonding in wafer-level has been achieved. The focused ion beam (FIB) technique has been used to inspect the bonding reliability. Transmission electron microscopy (TEM) was performed to confirm the atomic bonding across the Al_2O_3/SiO_2 interface. Atomic force microscopy (AFM), wettability, and X-ray photoelectron spectroscope (XPS) characterizations have also been adopted to study the bonding mechanism. Since Al_2O_3 has a large transparency window up to ~5.2 μm, this platform has broader sensing applications. To achieve the ultrahigh sensitivity, we built a theoretical framework for the signal enhancement to guide the device design based on the temporal coupled-mode theory (TCMT). Applying water as a proof-of-concept sample, experimental verification for device performance has been carried out. The issue of strong IR absorption of deionized water is bypassed thanks to the nanometer long optical paths. An *in situ* real-time dynamic monitoring for the molecular diffusion in water has also been presented. This continuous long-time detection process not only confirmed the high bonding quality but also showed ultrahigh sensitivity for liquid concentrations even with similar refractive indexes.

RESULTS AND DISCUSSION

The schematic diagram of the self-driven Al_2O_3-based plasmonic nanofluidic device is shown in Figure 1a. The tailored Au nanoantenna arrays are fabricated on the Al_2O_3 substrate, while the optical thickness Au film is deposited in the etched SiO_2 chamber to block the transmitted light. The analyte can spontaneously flow into the nanochannel and sensing chamber created by the direct bonding of patterned Al_2O_3 and SiO_2 under the action of capillary force. When the MIR light is incident on the nanoantenna arrays through the Al_2O_3 substrate, plasmonic resonances will be formed to couple with molecular vibrations. At the same time, inversed electrical field distributions are excited on the opposite nanoantennas and Au reflective film to generate quadrupole resonances, as shown in Figure S1. Therefore, the whole space which will be occupied by the liquid to be tested can be utilized to enhance the signal. However, this quadrupole resonance mode is easily affected by the gap distance, as shown in Figure S1a-i,b-i. The working mode can be converted to the dipole resonance, and the electric field can also be weaker when the gap distance is too large. Moreover, the vertically enhanced hotspots enable a higher sensitivity compared with the dipole-resonance plasmonics. Additionally, the magnetic dipole induced by the circulating current can be observed, as shown in Figure S1a-ii,b-ii. This electromagnetic response causes a reduction in the radiation damping. Inspired by this phenomenon, we can tune the ratio of external (γ_r) to intrinsic (γ_a) loss rates by controlling the electromagnetic intensity depended on the gap distance. To understand more intuitively, we have extracted γ_r and γ_a from the simulated reflection spectra with different nanogaps according to the TCMT, as displayed in Figure 1b. The representative reflection spectra with and without analytes are shown in Figure 1c, while the detailed simulations and statistical results are presented in Figure S2 and Table S1, respectively. As the gap distance increases, there is an inverse change between γ_r and γ_a. The whole 3D plasmonic system is critically coupled when the external and intrinsic damping rates are equal. Meanwhile, the reflective resonance dip is also the strongest (*i.e.*, perfect absorption) at the designed wavelength, as shown in Figure 1c-iii. When the analyte flows into the sensing chamber, the molecular vibration does not strongly interact with the incident MIR light but can couple with the plasmonic resonators. Thus, the original quadrupole resonance is broken, making the reflection spectra change into the asymmetric Fano shape, as shown by the short-dash-dot line in Figure 1c. Correspondingly, detection signals can be calculated as the difference of the reflection changes. The detection sensitivity depends on the changed degree of spectra. Traditionally, the strongest detection sensitivity is usually achieved at the point of perfect absorption or the densest electric field. However, the largest change occurs in the under-coupled system rather than the critically coupled plasmonic resonator according to the simulation results, as shown in Figure 1c-ii. Although the electric fields are stronger as the nanogaps become smaller according to the simulated results shown in Figure 1e, the amount of the detected analyte is also reduced. Therefore, there is a trade-off between the electric field and the number of sensing molecules to achieve maximum sensitivity. Due to the accurate prediction of reflection spectra from TCMT of MIM structures, we can build up the theoretical framework of the enhanced molecular signals based on the TCMT to guide the device design. General equations of the coupled-mode theory can be described as follows:[45]

$$\frac{\mathrm{d}P}{\mathrm{d}t} = j\omega_0 P - (\gamma_a + \gamma_r)P + j\mu M + ks_+ \tag{1}$$

$$\frac{\mathrm{d}M}{\mathrm{d}t} = j\omega_m M - \gamma_m M + j\mu P \tag{2}$$

$$s_- = -s_+ + kP \tag{3}$$

$$R = \left|\frac{s_-}{s_+}\right|^2 \tag{4}$$

where P and M are the mode amplitude of the plasmonic structure and molecular vibration, ω_0 and ω_m are the resonance frequency of the plasmonic structure and molecular vibration, and μ is the coupling strength. R is the reflection spectra constrained by the amplitude of the input (s_+) and output (s_-) light, while k denotes an arbitrary factor related to γ_a (*i.e.*,$k = \sqrt{2\gamma_a}$).[26,45] By substituting eqs 1−3 into eq 4, the reflection spectra changes with the incident light (ω) can be obtained

$$R(\omega) = \left| \frac{j(\omega - \omega_0) + (\gamma_a - \gamma_r) - \frac{\mu^2}{j(\omega - \omega_m) + \gamma_m}}{j(\omega - \omega_0) + (\gamma_a + \gamma_r) + \frac{\mu^2}{j(\omega - \omega_m) + \gamma_m}} \right|^2 \tag{5}$$

Practically, the detected signals are expressed as the differences of reflection spectra with and without analytes

$$\Delta R = R - R|_{\mu=0} \tag{6}$$

When $\omega = \omega_0 = \omega_m$, the highest sensitivity will be achieved. The expression of the molecule signals can be obtained by substituting eq 5 into eq 6

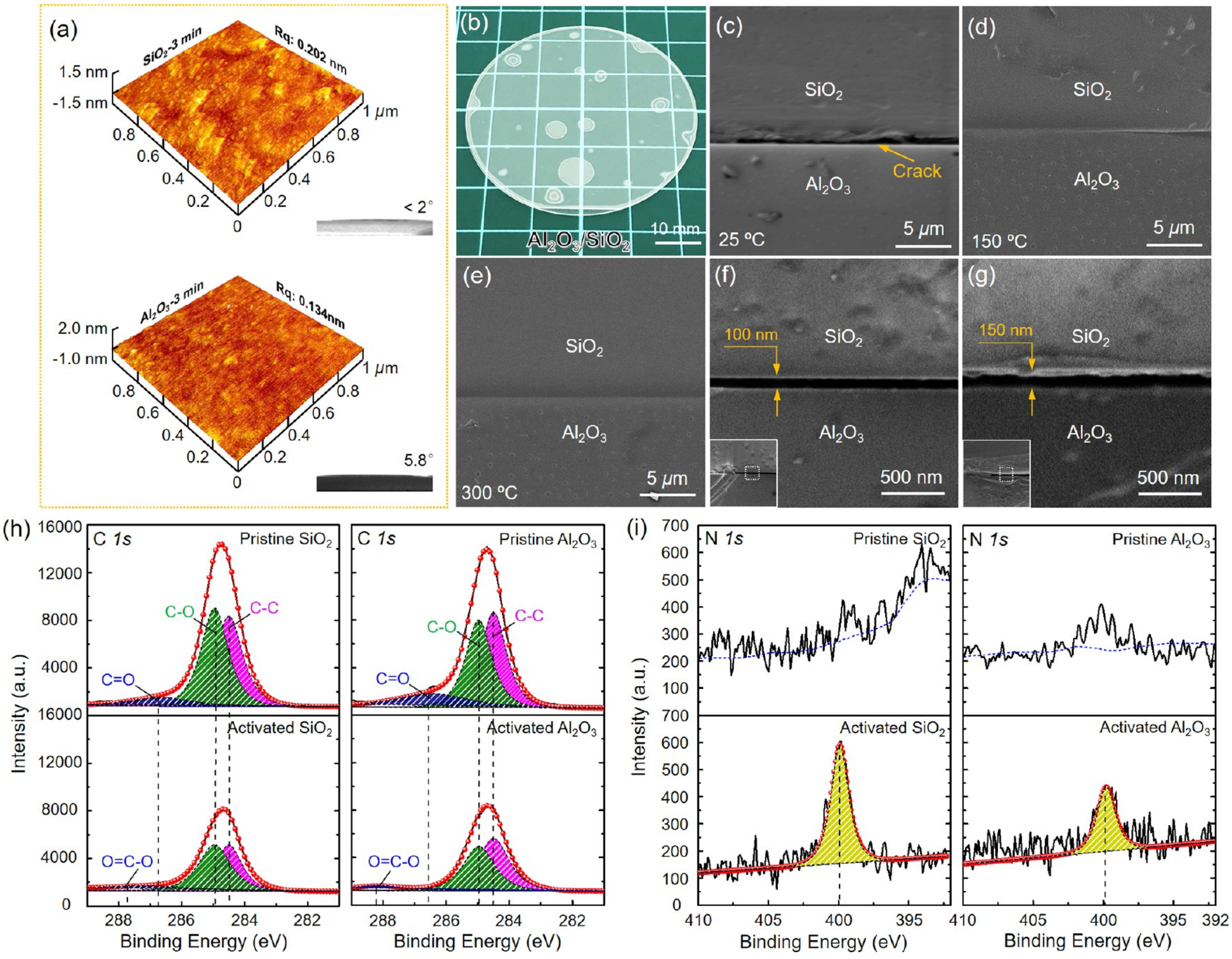

Figure 2. Surface and interface characterizations for Al_2O_3/SiO_2 direct bonded pairs: (a) 3D AFM images of the plasma-activated SiO_2 and Al_2O_3 surfaces. The inserts are the corresponding water contact angle images. (b) Optical image of the Al_2O_3/SiO_2 direct bonded pairs at wafer-level. (c) Al_2O_3/SiO_2 bonding interface without annealing. SEM images of Al_2O_3/SiO_2 bonding interface annealed at (d) 150 °C and (e) 300 °C. (f) 100 nm and (g) 150 nm nanocavities created by Al_2O_3/SiO_2 direct bonding. The inserts in (f) and (g) are the cross sections of nanocavities that simultaneously show the bonding regions and nanogaps. Comparison of XPS spectra for the SiO_2 and Al_2O_3 substrates before and after the plasma activation: (h) C 1s core spectra and (i) N 1s core spectra.

$$\Delta R = \left|\frac{\gamma_r - \gamma_a'}{\gamma_r + \gamma_a'}\right|^2 - \left|\frac{\gamma_r - \gamma_a}{\gamma_r + \gamma_a}\right|^2 \quad (7)$$

where $\gamma_a' = \gamma_a + \mu^2/\gamma_m$. Thus, the dark mode of this system can be thought of adding an amount of additional intrinsic damping loss to the bright mode, resulting in a leftward movement for the reflection dip along the reflection curve,[26] as shown in Figure S2. By fitting the reflection spectra according to the TCMT, we can find that $f' = \gamma_r/\gamma_a'$ is approximately linear to f (*i.e.*, $f' \cong tf$), as shown in Figure S3. So we can relate the molecule signals with the normalized radiative loss as (detailed equation calculations are shown in Note S3)

$$\Delta R \propto \frac{(tf^2 - 1)(t - 1)f}{(tf + 1)^2(f + 1)} \quad (8)$$

The reflection dip and enhanced molecular signals for the plasmonic nanofluidics as a function of γ_r/γ_a are shown in Figure 1d-i,ii, respectively. The spheres are the simulated results by the finite-difference time-domain (FDTD) method at different nanogaps. They fit well with our calculated theoretical curves. Then, we carried out a series of experiments to verify its accuracy further.

To fabricate the Al_2O_3-based MIR sensing platform, direct bonding of Al_2O_3 and SiO_2 is an essential process for the device sealing and nanogap control. Because gold (Au) nanoantennas will be embedded into the nanofluidics, bonding performed at complementary metal-oxide-semiconductor (CMOS)-compatible temperatures is necessary to protect the metal shapes. According to the previous studies, fluorine (F)-[46−48] or nitrogen (N)-[34,49−51]contained plasma can be more effective in modifying surfaces and strength bonding interfaces. Here, we developed an $NH_3/O_2/H_2O$ plasma-activated low-temperature direct bonding method for Al_2O_3 and SiO_2. After 3 min of plasma activation, both Al_2O_3 and SiO_2 surfaces become very smooth and hydrophilic, as shown in Figure 2a. These changes are beneficial for direct bonding,[35,52−54] and Al_2O_3/SiO_2 bonding in wafer-level has been achieved, as shown in Figure 2b. Annealing at 300 °C for 12 h can keep the bonding interface tight and void-free, while

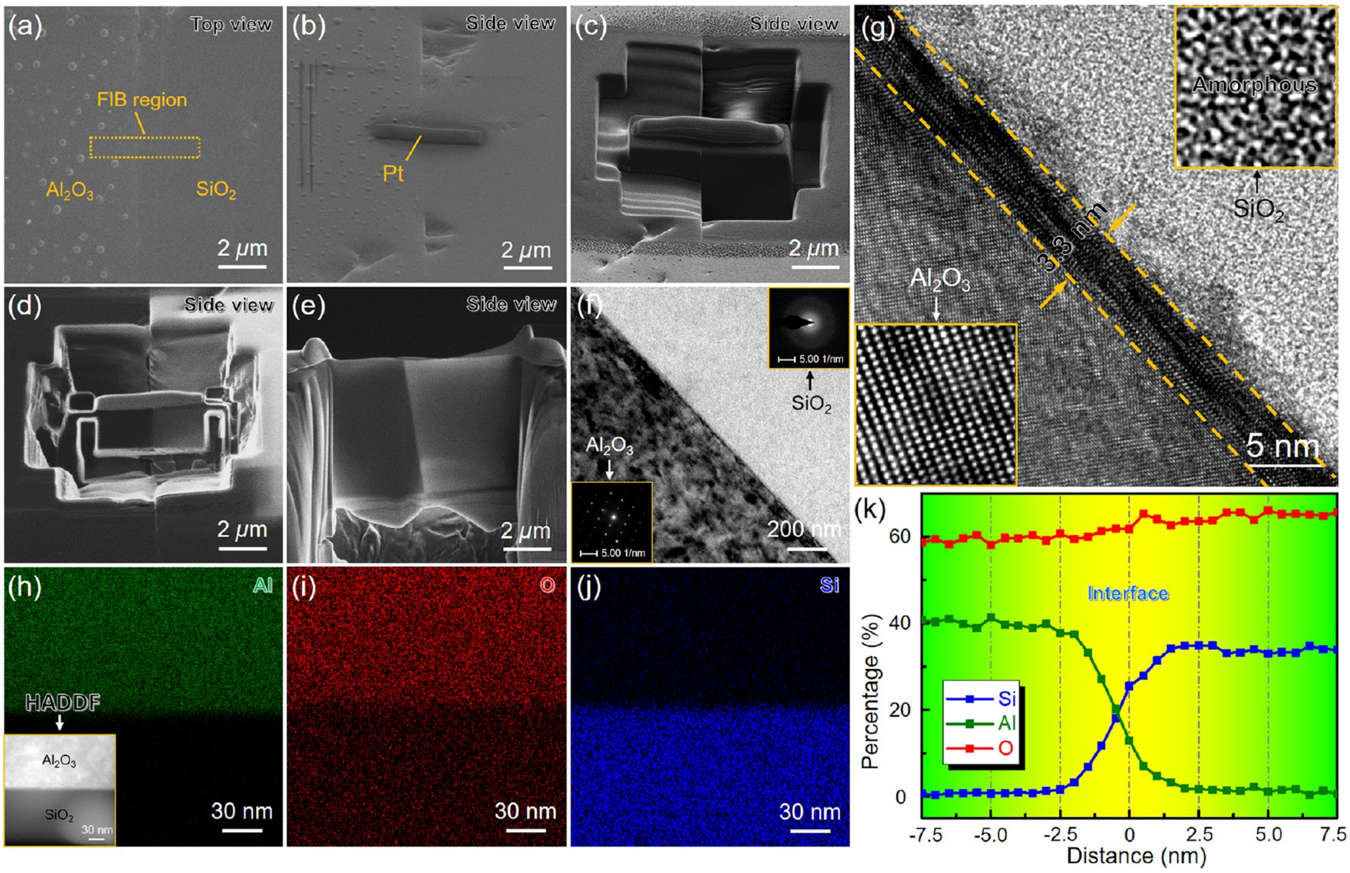

Figure 3. TEM observation of the Al_2O_3/SiO_2 direct bonding interface. (a−e) TEM sample fabrication process by FIB technique. The Al_2O_3/SiO_2 bonding interface is bombarded with a Ga ion beam for 6 h to obtain the ultrathin sample for TEM observation. It also confirms that the bonding strength is strong enough to withstand the mechanical and thermal stress during the FIB process. (f) Bright-field image of the bonding interface. Inserts show the selective electron diffraction patterns of Al_2O_3 and SiO_2 substrates closed to the interface. (g) HRTEM image of the bonding interface. The bonding interface is 3.3 nm in thickness, which ensures accurate control of the gap distance in Al_2O_3/SiO_2 plasmonic-nanofluidic devices. (h−j) EDX mappings of Al, O, and Si elements. The insert in (h) is the HADDF image of the interface. (k) EDX line scanning across the bonding interface. The smooth transition of elements confirms sufficient diffusion to get a reliable interface.

the bonded pairs stored at room temperature and annealed at 150 °C show the cracked and uneven interfaces, as shown in Figure 2c−e. It is mainly because the annealed bonded pairs have strong bonding strength, which could resist the thermal stress, water stress corrosion, and mechanical stress during the scanning electron microscopy (SEM) sample preparation. We also performed the "crack opening" method to measure the bonding strength. The heterogeneous surface energy (γ) is calculated using the following equation:

$$\gamma = \frac{3{t_b}^2 E_1 {t_{w1}}^3 E_2 {t_{w2}}^3}{16L^4(E_1 {t_{w1}}^3 + E_2 {t_{w2}}^3)} \tag{9}$$

where E_1 and E_2 are the Young's moduli for sapphire (4×10^{11} Pa) and SiO_2 (6.6×10^{10} Pa), respectively, t_{w1} and t_{w2} are the thicknesses of sapphire (500 μm) and SiO_2 (500 μm) wafers, t_b is the blade thickness (100 μm), and L is the crack propagation length. The measured optical image can be seen in Figure S4, showing the crack propagation length is 3.96 mm. Therefore, the calculated bonding energy is 2.1 J/m^2.[55] To further ensure the bonding reliability, we also bonded the SiO_2 samples with different etching depths and bare Al_2O_3 substrates. The nanogaps with accurate distance and ideal sealing created by the direct bonding are shown in Figure 2f,g. Therefore, we have strong evidence that our bonding method is reliable. Moreover, we also utilized XPS to study the mechanism of enhanced bonding strength. $NH_3/O_2/H_2O$ plasma activation has two benefits for the surfaces to be bonded. First, the mixed plasma can effectively clean surfaces. Compared with the pristine Al_2O_3 and SiO_2 surfaces, organics adsorbed on the plasma-activated surfaces are removed according to the C 1s spectra, as shown in Figure 2h. It will significantly improve the bonding ability and bonding areas. Second, N-related chemical bonds hang on the activated surfaces to be bonded when compared to the N 1s spectra before and after the mixed plasma activation, as shown in Figure 2i. It plays an important role in strengthening the bonding interfaces due to the binding energies of $\equiv$Si−N= and $\equiv Si_2$−N− bonds are stronger than the $\equiv$Si−O− bond across the interfaces.[34] For the other core spectra of SiO_2 and Al_2O_3 substrates, chemical bonds associated with the bonded substrates remain almost unchanged, as shown in Figure S5, indicating that the mixed plasma does not significantly damage the materials.

TEM observation for the Al_2O_3/SiO_2 bonding interface is also conducted. To fabricate the TEM sample, the FIB technique is performed, as shown in Figure 3a−e. The bright-field image indicates that the interface remains defect-free even after ∼6 h bombardment with a gallium (Ga) ion beam, as shown in Figure 3f. High-resolution TEM (HRTEM) images

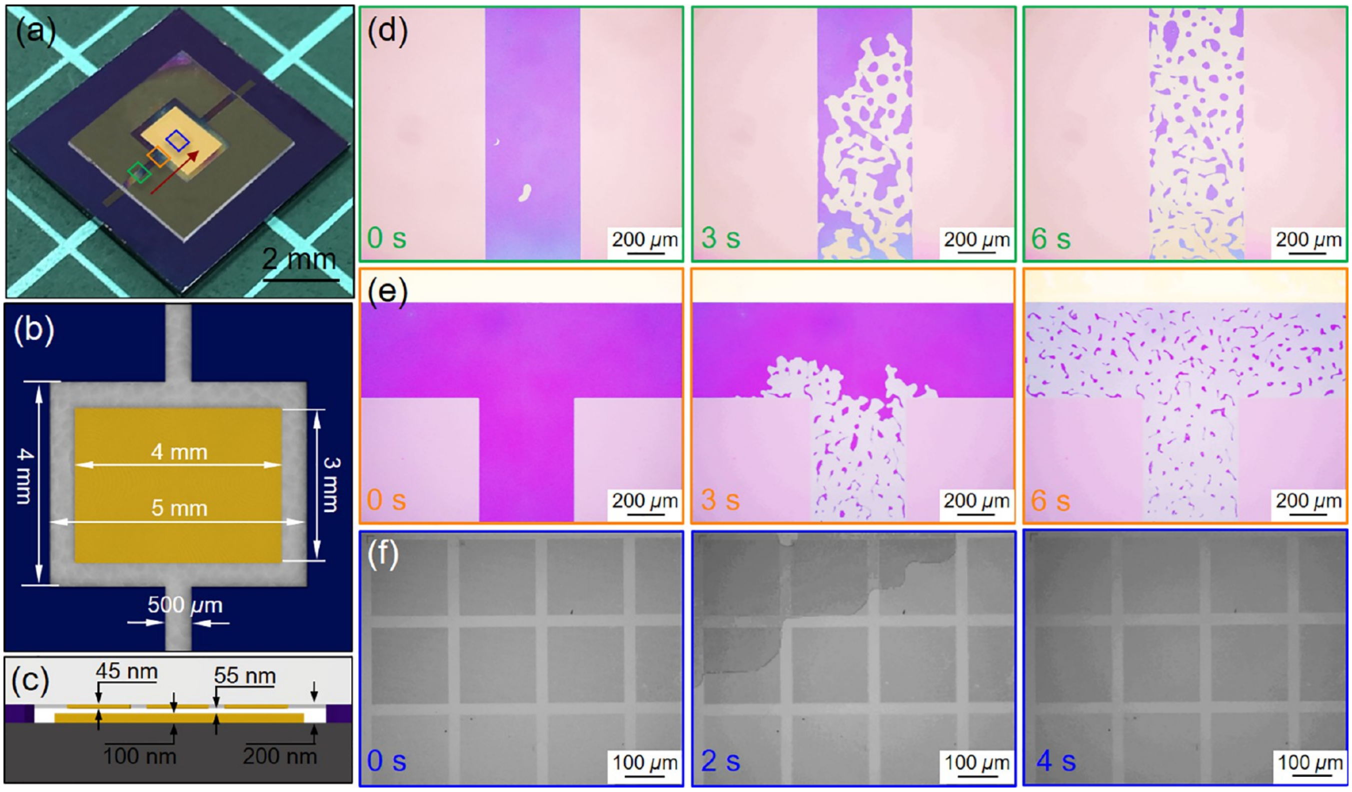

Figure 4. Capillary force test with DI water. (a) Optical image of the fabricated Al_2O_3-based 3D plasmonic sensing platform. (b) and (c) Dimensions and structural configurations for the device with a 55 nm nanogap. The DI water flows into the (d) nanochannel, (e) intersection, and (f) sensing chamber under the effect of capillary force. The DI water has been well confined in the nanochannel and sensing chamber due to the high-quality bonding. The whole dynamic process has been recorded by the microscope, as shown in Movie S1.

of the interface show that atomic bonding has been achieved, as shown in Figure 3g. The transition layer is 3.3 nm, which is also the maximum error for nanogaps caused by the bonding. Such a small error can ensure the precise control of the gap distance. Besides, the diffraction spots inserted in the image in Figure 3f and the enlarged region in HRTEM indicate that the single-crystal structure of the Al_2O_3 substrate is not destroyed. This can maximize the optical properties of Al_2O_3 during the sensing process. The energy dispersive X-ray (EDX) mappings and line scanning also demonstrate that atoms form a gradient diffusion across the bonding interface, as shown in Figure 3h–k. Based on the above analyses, our proposed bonding method has obvious characteristics in exerting the performance of optical materials, accurately controlling nanogaps, and reliable device sealing.

Optical images of the plasmonic-nanofluidic assembled by the mixed plasma-activated direct bonding are shown in Figure 4. Perfect bonding for the device deposited with metal objects has been realized, as shown in Figure 4a. The dimension for the device with a 55 nm nanogap is shown in Figure 4b,c. During the capillary force test, deionized (DI) water is dropped at the entrance. The sealed channel can produce capillary force, driving the liquid into the sensing chamber. The whole spontaneous process has been recorded by the microscope (see Movie S1). Figure 4b–d shows the time-dependent liquid flow at different locations. It can be seen that the bonding interface remains intact and does not crack even with water erosion. Due to the high-quality bonding, the liquid is also well confined in the channel and chamber, which ensures the device stability during the performance measurements. It is worth noting that there are many tiny air gaps during the rapid filling of the nanochannel with water. These air gaps are mainly due to the rough surface caused by the etching process. The liquid will infiltrate the entire space after a few minutes.

Figure 5a presents the SEM images of Au nanoantennas with different lengths fabricated on Al_2O_3 substrates. To obtain well-formed and stable nanoantenna arrays, 5 nm titanium (Ti) is first deposited as the adhesion layer and followed by a 40 nm-thick Au layer using the electron-beam evaporator. The period of each unit cell is 1.5 μm. To check our proposed signal enhanced theoretical framework, we fabricated the Al_2O_3-based sensing platforms with different nanogaps and choose DI water as a proof-of-concept analyte, since the strongest spectra recovery occurs when the near-field coupling is aligned to the analyte absorption peak. Therefore, different nanoantenna lengths with a fixed width of 200 nm are used to tune the reflection spectra to make the resonance peak coincide with the absorption peak of DI water. SiO_2/Si substrates are also etched to different depths to create different nanogaps. Atomic force microscopy (AFM) and surface profiler are used to characterize the cross-sectional profiles for Au antennas and etched SiO_2, respectively, as shown in Figure S7. Therefore, it can be calculated that the nanogaps formed in different sensing chambers are 30, 55, 90, 140, and 165 nm. Figure 5b shows the measured results of nanoantenna arrays without the Au mirror. With the increase of nanoantenna length, the resonant peak shifts linearly. The shifts are originated from the feed-gap impedance related to the nanoantenna length. When the metasurfaces equipped with the Au mirror deposited at the bottom of the SiO_2 chamber, there is an inversion occurred on the resonant peak. Figure 5c

https://dx.doi.org/10.1021/acsnano.0c05794
ACS Nano 2020, 14, 12159−12172

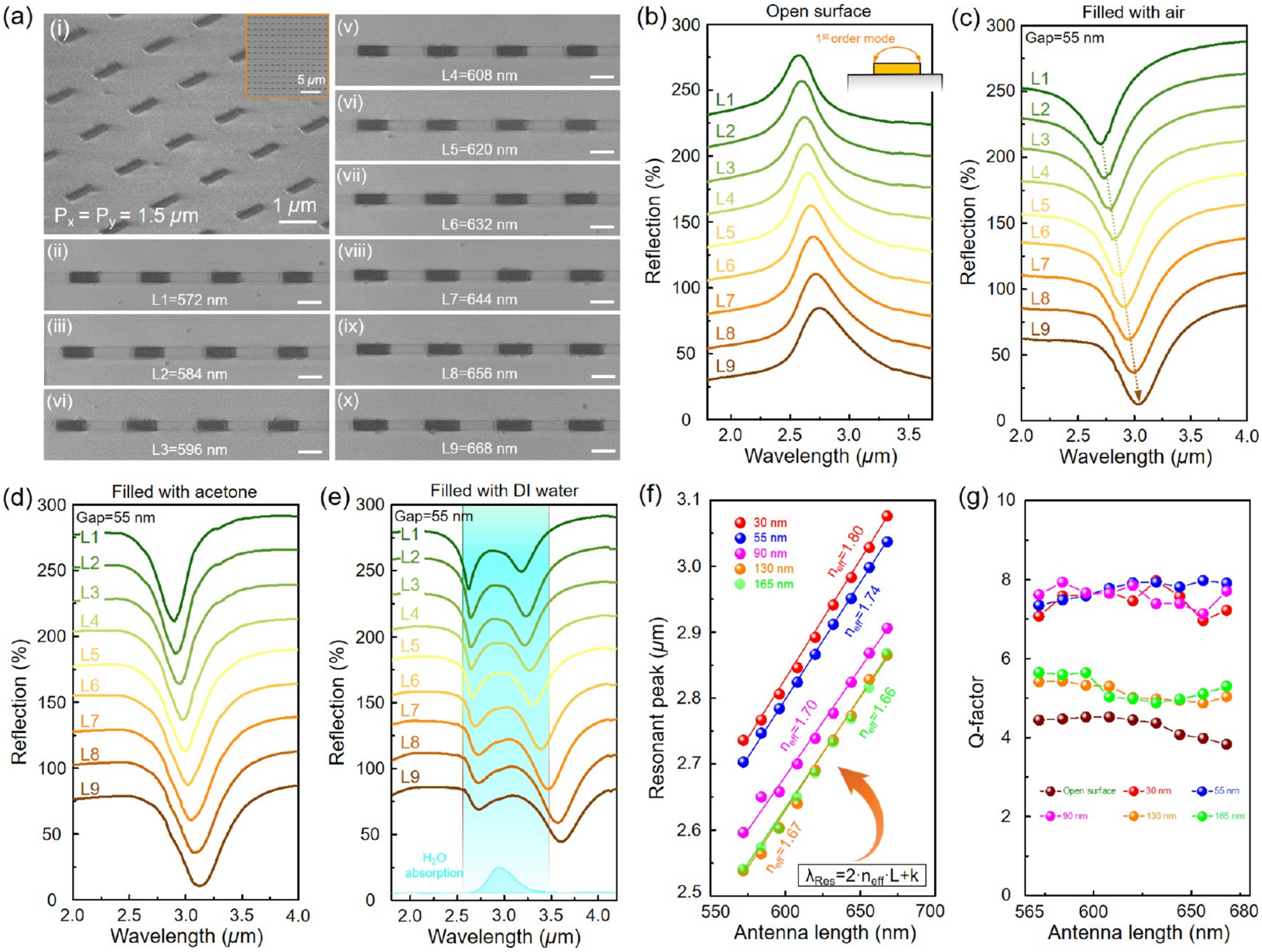

Figure 5. Spectra tuning and H_2O signal detection. (a) SEM images of different antenna lengths with a period of 1.5 μm. The lengths are varied from 572 to 668 nm with an interval of 12 nm. Measured reflected spectra at different antenna length arrays (b) without and (c) with Au reflected chamber surrounded by air. Absorption spectra with Au reflected chamber filled by (d) acetone and (e) DI water at different lengths of antennas. The gap distance between Au antennas and the mirror is 55 nm. The measured reflected spectra filled with air and DI water in the chamber with 30, 90, 130, and 165 nm gap distances are shown in Section S5. (f) Relationships between antenna length and resonant peak with Au reflected chamber at different nanogaps. The bright dots are the statistical experimental data. The slope lines are the fitting results. (g) *Q*-factors of the measured reflected spectra at different nanogaps.

shows the reflection spectra of the 55 nm nanogap filled with air between the nanoantennas and the Au mirror. The reflection spectra at 30, 90, 140, and 165 nm nanogaps filled with air are shown in Figure S6a-i,b-i,c-i,d-i, respectively. It can be seen that the resonance is successfully overlapped with the O−H stretching band of DI water whose absorption covered from 2.5 to 3.5 μm. All resonant wavelengths vary linearly with different scaling factors as the nanoantenna length changes. The statistical results are shown in Figure 5f. The effective refractive index (n_{eff}) is used to calculate the inhomogeneous dielectric environment (including substrates and analytes) surrounding the nanoantennas.[56] Due to the changes in the gap distances, larger gaps will contain more liquid with a lower refractive index, resulting in a slight decrease in the scaling factors. Compared with the open surfaces, a larger resonant peak with higher quality (*Q*)-factor is achieved when the antenna arrays equipped with Au mirror, as shown in Figure 5g. It is mainly due to the stronger intensity of the quadrupole resonance mode produced between nanoantennas and mirror, as the simulated results are shown in Figure S1. Correspondingly, the plasmonic nanofluidic devices can show more sensitivity. Moreover, compared with overcoupled plasmonic structures (130 and 165 nm nanogaps), the under-coupled (30 and 55 nm nanogaps) and near critically (90 nm nanogap) coupled systems show higher *Q*-factors because of stronger quadrupole resonance mode. Before we introduce the DI water for the signal enhancement analysis, we chose acetone as the reference sample, since acetone shares a similar real part of the refractive index with DI water, while has a tiny imaginary part in the wavelength range of 2.5−3.5 μm. Compared with the device filled with air, the reflection dip had a ∼2.0% increase in transmittance and a 100 nm red-shift in the central resonance wavelength when the device filled with acetone. Both of them are caused by the refractive index change, making the damping rate different.[57] Therefore, choosing the reflection spectra measured with acetone as the reference will make the signal enhancement analysis more accurate. Subsequently, we replace acetone with DI water. The measured spectra of the 55 nm nanogap device filled by DI water are shown in Figure 5e. The reflection spectra at 30, 90, 140, and 165 nm nanogaps filled

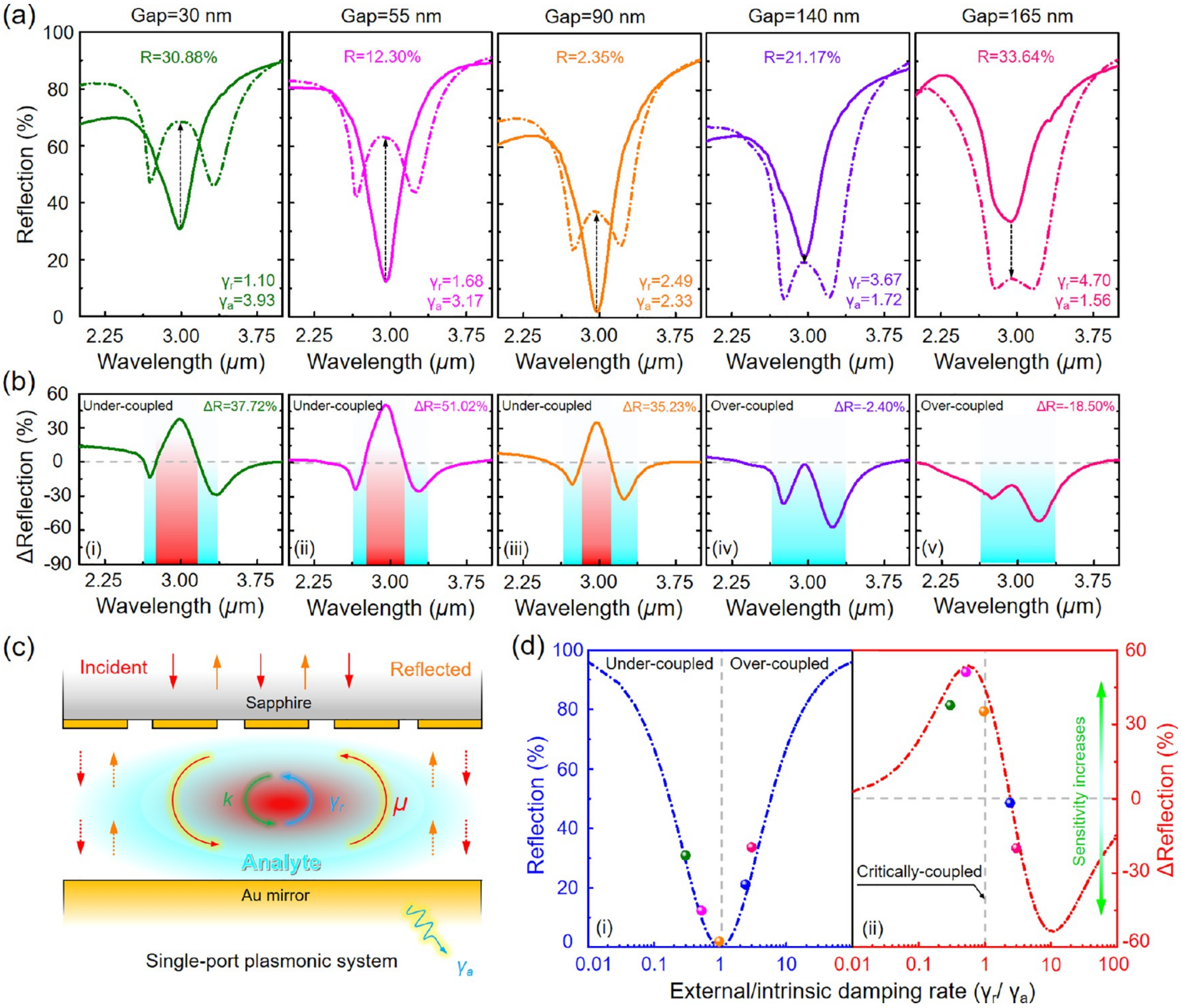

Figure 6. Comparison of the signal enhancement at different nanogaps. (a) Measured spectra filled with acetone and DI water in Au reflected chamber at different gap distances. Acetone has a similar refractive index with DI water, and acetone has no obvious absorption peak at 2.5–3.5 μm. To avoid to reflection difference induced by different refractive indexes, we choose spectra measured with acetone as the references. (b) Spectra differences induced by water absorption at different nanogaps. (c) Schematic diagram of the coupling principle for the single-port plasmonic system. (d) Comparison of the experimental results with our proposed theoretical curves.

with DI water are shown in Figure S6a-ii,b-ii,c-ii,d-ii, respectively. Obvious recoveries of the reflection have been observed. The asymmetric Fano-shaped curves vary orderly when the resonant peak of antenna arrays gradually changed from lower to higher wavelength than the DI water central absorption peak.

To intuitively compare our proposed signal enhancement theory with the experimental results, we extracted the reflection spectra as the resonance dips generated by the specific nanoantenna lengths are aligned to the DI water absorption. The spectra measured with acetone (solid line) and DI water (short-dash-dot line) at different nanogaps are shown in Figure 6a. The peak reflections without analyte absorption are 30.88%, 12.30%, 2.35%, 21.17%, and 33.64% corresponding to the nanogaps of 30, 55, 90, 140, and 165 nm, respectively. These experimental results fit well with the derived theoretical curve about the reflection without absorption, as shown in Figure 6d–i. Changes in reflection spectra are mainly affected by two aspects after replacing acetone with DI water. One is the vibrational absorption of water molecules, and the other one is the resonant strength in near- and far-fields, as the diagram shown in Figure 6c. When the plasmonic system only considers the vibrational absorption, the reflection of the resonant peak at each wavelength will be reduced.

Meanwhile, the original quadrupole resonance is broken, making the reflection increase. Therefore, the reflection spectra with analyte are jointly affected by the analyte absorption and resonant strength of the plasmonic system. When the influences of deresonance are stronger than the molecular absorption, the reflection will improve compared with the system without absorption. On the contrary, changes in the spectra will reverse. The differences in spectral measured with DI water and acetone are presented in Figure 6b. The

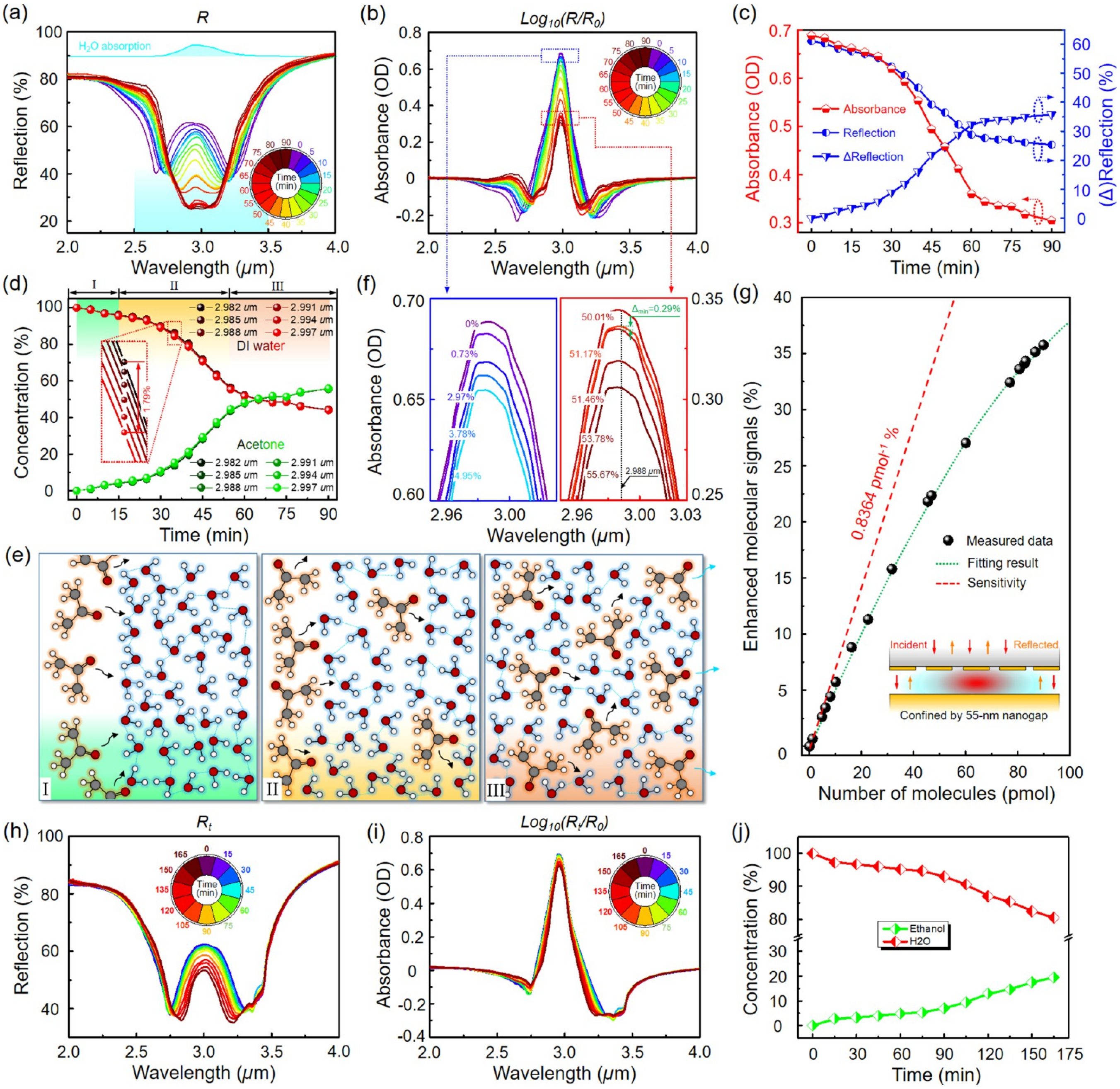

Figure 7. *In situ* dynamic monitoring for molecular diffusion in DI water. (a) Measured infrared spectra during the acetone molecular diffusion in DI water at different times. The measurement was performed every 5 min. (b) Differential absorption spectra calculated from (a). (c) Statistical results of absorbance, reflection peak, and reflection differences at different times. (d) Concentration changes along with diffusion time. The concentration is calculated from the absorbance shown in (c). To show the accuracy of concentration calculation, conversion results of absorbance are plotted at different wavelengths. The inset shows the maximum deviation (1.79%) of the calculated concentrations. (e) The schematic diagram of the acetone diffusion mechanism in nanoconfined space. (f) Enlarged views of curves in (b) show the clear distinction for liquid even with similar concentrations. The smallest acetone concentration change that can be distinguished is 0.29%. The extracted data are from a fixed wavelength of 2.988 *μ*m. (g) Experimentally molecular signal enhancement *versus* the number of acetone molecules. The green dot line shows the fitting curve, and the red dashed line shows the sensitivity up to 0.8364 pmol^{-1} % of this Al_2O_3-based platform at low concentrations. (h) Measured reflection spectra during the ethanol molecular diffusion in DI water at different times. (i) Differential absorption spectra converted from (h). (j) Changes of ethanol concentration at different diffusion times.

plasmonic system possesses strong quadrupole resonances, but a little analyte when the nanogaps are small. Therefore, the deresonances are stronger than the absorption in the near-field wavelength region, making the reflection increase, as shown in the red shaded area in Figure 6b-i–iii. Unfortunately, the resonances become weak in the far-field, and the analyte absorption dominates the spectra, resulting in decreases in reflection, as shown in the blue shaded area. As the nanogap becomes large, the plasmonic system will transfer from under-coupled to overcoupled situations. At this time, the number of analytes increases, while the resonance weakens even in the near-field wavelength. Thus, the absorption plays a leading role, causing the reflection to reduce in the whole resonance wavelength, as shown in Figure 6b-iv,v. This is also the reason that the spectra with analyte become broadened. Additionally, changes in the peak reflection obtained from the spectral differences are 37.72%, 51.02%, 35.23%, 2.4%, and 18.50% at different nanogaps. They are well-matched with our theoretical predictions, as shown in Figure 6d-ii. It can be seen that the signal enhancement is easily affected by the damping rates. Therefore, it is important to choose a proper gap distance to optimize device performance. To show the ultrahigh sensitivity of this platform, we have performed an *in situ* concentration study using this plasmonic nanofluidic with a 55 nm nanogap.

Phenomena of mass transport by diffusion are ubiquitous in chemical and biological science and engineering.[58,59] Among them, molecular diffusion in hydrogen-bonding associated system has always been recognized as a challenging problem.[60,61] However, few studies have been reported to learn molecular diffusion in nanoscale. Combining the advantages of our Al_2O_3-based 3D sensing platform, we have conducted a real-time observation for the acetone molecular diffusion in DI water in nanospace. Currently, the working mechanism of most plasmonic sensors is based on the changes in the refractive index.[62−64] Unfortunately, for liquids with similar refractive index, these devices have low sensing resolutions for concentration detection. The plasmonic nanofluidic, which depends on the reflection changes, can solve this problem. Therefore, we choose DI water and acetone to verify it. First, we drop 1 μL of DI water at the device entrance. When DI water fills the whole sensing chamber, the first spectral test is performed. Simultaneously, the acetone is dropped at the device entrance to begin the diffusion process. Since the device has already been filled with DI water, acetone can be considered as a quasi-static diffusion in DI water without the effect of the capillary force. Since liquid diffusion is a time-consumption process,[65−67] we perform the spectral tests with a 5 min time interval to make the diffusion results closer to the actual situation. The whole process lasts 90 min, and the measured reflection spectra are shown in Figure 7a. The spectra have gradually changed along with the diffusion time. To aid the subsequent concentration analysis, the reflection spectra are converted to the differential absorption, as shown in Figure 7b. The absorbance signals are computed as

$$A = \log_{10}\left(\frac{R}{R_0}\right) \tag{10}$$

where A is the absorbance, and R and R_0 are the spectra measured with and without analyte absorption, respectively.

The statistical results of absorbance, reflection peak, and reflection differences at different diffusion times are plotted in Figure 7c. It can be found that the varied rate in absorbance or reflection first increases slowly, then accelerates, and finally slows down again. To intuitively observe the concentration changes, we set A_0 corresponding to the first spectrum measured from 100% DI water. Concentrations for DI water and acetone at other times are calculated as

$$C_{H_2O}^{t} = \frac{A_t}{A_0} \times 100\% \tag{11}$$

$$C_{acetone}^{t} = 1 - C_{H_2O}^{t} \tag{12}$$

where $C_{H_2O}^{t}$ and $C_{acetone}^{t}$ are the concentrations for DI water and acetone, respectively, and A_t is the absorbance changes with the diffusion time. To confirm the accuracy of concentration calculations, we select the absorbances at several wavelengths to compare the converted results. The concentration changes are shown in Figure 7d. The enlarged view shows that the maximum deviation occurs, which is only 1.79% when the diffusion duration reaches to 50 min. This proves that our calculation method possesses a high accuracy. Considering the changing trend of acetone concentration, there are three stages during the diffusion in nanospace. The H_2O molecule primarily consists of hydroxyl (−OH) groups, which possess strong polarity.[68,69] One molecule can form up to four hydrogen bonds with adjacent H_2O molecules. Thus, the complex hydrogen-bonding cross-linked network has excellent resistance to acetone, making the diffusion slow, as indicated in Figure 7e-i. Because the acetone molecule only has one proton-accepting carbonyl group that can form hydrogen bonds with proton-donating groups from water,[70] the hydrogen-bonding framework will be partly destroyed when the diffusion continues. As the acetone concentration is more than ∼4.01%, acetone molecules gradually split the original hydrogen-bonded associations formed by water, as indicated in Figure 7e-ii. Therefore, the diffusion resistance is reduced, and the diffusion speed is accelerated. Such a phenomenon repeatedly occurs until the acetone concentration reaches ∼44.48%. However, the diffusion rate begins to decrease as the acetone concentration further increases. Due to the strong volatility of acetone, the evaporation rate will also increase along with the acetone concentration. The rapid evaporation of acetone might affect further diffusion, as indicated in Figure 7e-iii. Consequently, there is a balance in the concentration changes. Figure 7f presents the enlarged view of curves in (b). Clear distinctions for liquids, even with similar concentrations, are shown. The smallest concentration change that can be distinguished is 0.29%, which was nearly 2 orders of magnitude than currently reported sensitivity for detecting the same molecule.[23,71] Due to the ultrasmall sensing chamber, quantitative analyte analysis can be performed in this kind of plasmonic-enhanced nanofluidic device. Therefore, we convert the acetone concentrations in the dynamic test into the number of molecules. The relationship between the enhanced molecular signal and the number of molecules is shown in Figure 7g. The detailed calculation for the number of acetone molecules can be seen in Note S9. By fitting changes in the number of molecules and spectral reflection, we can obtain the detection sensitivity, which was up to 0.8364 $pmol^{-1}$ %. Thus, we can confirm that this Al_2O_3-based platform enables the real-time dynamic molecular diffusion studies with ultrahigh sensitivity.

As we all know, the absorption band of acetone is negligible in the range of 2.5−3.5 μm because its imaginary part of the refractive index (k) is almost zero. DI water has a strong absorption in the wavelength of 2.5−3.5 μm. Therefore, it is easy to distinguish changes in the absorbance caused by different acetone concentrations. In fact, the working principle of the plasmonic nanofluidic depends on the detection of the k, which is considered as the IR fingerprint absorption of O−H. Changes in the liquid concentration induce different absorbance as long as the k of the solute is not the same as that of DI water in the range of 2.5−3.5 μm. Taking ethanol as an example, this molecule also contains O−H functional group and performs the same absorption peaks at 3.0 μm. In the HN-SEIRA platform, it is able to detect the ethanol concentration in water without limitation because our sensing method only depends on the *k*. A diffusion test of ethanol is conducted to validate the feasibility. The measured spectra of acetone, DI water, and ethanol are shown in Figure S10a,b,d, respectively. The acetone is used to provide a reference signal to compensate for the red-shift of nanoantenna caused by a refractive change of liquid since it does not absorb IR light at 3.0 μm and perform similar refractive index to DI water and ethanol. The corresponding converted differential absorption spectra are presented in Figure S10c,e. They are also used to calibrate the ethanol concentration as 0% and 100%, respectively. The reflection spectra during the ethanol diffusion are recorded in Figure 7h. To simplify the analysis of concentration changes, both differential absorption conversion and statistics of peak values are performed, as shown in Figure 7i and Figure S10f, respectively. Due to ethanol has an absorption band in the range of 2.75−3.25 μm, its absorption signal is not zero when the ethanol concentration is 0%. Therefore, we need to use the following equations to convert differential absorption spectra into concentrations. The calculations can be performed as follows:

$$C^{t}_{\mathrm{ethanol}} = \frac{A_{\mathrm{H_2O}} - A_t}{A_{\mathrm{H_2O}} - A_{\mathrm{ethanol}}} \times 100\% \tag{13}$$

$$C^{t}_{\mathrm{H_2O}} = 1 - C^{t}_{\mathrm{ethanol}} \tag{14}$$

where C^{t}_{ethanol} and $C^{t}_{\mathrm{H_2O}}$ are the ethanol and DI water concentration changes along with diffusion time, respectively. $A_{\mathrm{H_2O}}$ and A_{ethanol} are the absorbance signals of DI water and ethanol and is shown in Figure S10b,d, while A_t is the absorbance signals at different diffusion times shown in Figure 7i. After the aforementioned calculations, the concentration changes during the ethanol diffusion process are recorded in Figure 7j. With the increase of diffusion time, the concentration of ethanol gradually changes. According to the results of dynamic monitoring experiments for acetone and ethanol in water, it shows the successful dynamic concentration detection where our technology is irrelevant to the absorption behavior of molecules in the measured absorption band.

CONCLUSION

In summary, we demonstrated an HN-SEIRA sensing platform with ultrahigh sensitivity. A plasma-activated method for low-temperature wafer direct bonding of sapphire and SiO_2 was developed to fabricate this platform, providing a possibility for the mass production of devices. A 3 min plasma activation could lead to ultrasmooth and hydrophilic surfaces, which were beneficial for wafer-level direct bonding. Strong and ultrathin (3.3 nm) interfaces have been confirmed by the cross-sectional sample fabrication and TEM observation. A theoretical framework for signal enhancement was proposed to guide the device design. By integrating plasmonics into nanofluidics with accurate nanogap control, loss engineering for the quadrupole resonance system has been theoretically studied and experimentally validated due to the high-quality sapphire bonding. With the action of the capillary force, the analytes could be spontaneously driven into the sensing chamber without additional actuation systems. An *in situ* real-time dynamic monitoring for the acetone molecular diffusion in DI water has been studied. Even small concentration changes (0.29%) in the diffusion process could be distinguished, indicating that this platform still possessed an ultrastrong detected capability even for the liquids with similar refractive indexes. The ability of quantitative molecular measurement was also demonstrated, and ultrahigh sensitivity of up to 0.8364 pmol^{-1} % has been achieved. Therefore, this HN-SEIRA sensing platform has great potential for chemical and biological dynamic analyses with ultrahigh sensitivity in MIR.

METHODS

Development of Al_2O_3/SiO_2 Wafer Direct Bonding. In the exploration of Al_2O_3/SiO_2 direct bonding, double-side-polished, 2 in. SiO_2 and (0001)-oriented Al_2O_3 wafers with thicknesses of 500 μm were used in the experiments. $O_2/NH_3/H_2O$ plasma was performed to active Al_2O_3 and SiO_2 wafer surfaces. To get $O_2/NH_3/H_2O$ plasma, the plasma equipment was modified, as shown in Figure S8. O_2 with a purity of 99.99% came from the oxygen cylinder, while NH_3 and H_2O gases were generated from the heated ammonia solution. The ratio of ammonia solution to deionized (DI) water was 1:3 in volume. The pressure in the chamber was set as 50 Pa when the plasma equipment was operating. Therefore, the mixture of water vapor and NH_3 could flow into the plasma chamber at 75 °C due to the low saturated vapor pressure. The flow rates of both O_2 and NH_3/H_2O were controlled at 10 sccm. After 3 min plasma activation, the activated Al_2O_3 and SiO_2 wafer surfaces were contacted to form prebonded pairs. Then, the Al_2O_3/SiO_2 prebonded samples were stored in the atmospheric environment for 24 h to saturate the prebonding strength. Finally, annealing at 300 °C for 12 h was conducted to promote the formation of covalent bonding across the bonding interfaces. Therefore, the bonding strength was strong enough to withstand the mechanical and thermal stresses as well as the water stress corrosion during the device dicing and performance tests.

Materials Characterization. The surface morphologies and roughness were recorded by an AFM (Dimension FastScan, Bruker) with an area of 1 × 1 μm^2. The wettability of plasma-activated sample surfaces was measured by a contact angle tester (OCA 25-HTV, Data Physics). Field emission scanning electron microscopy (Regulus8100, HITACHI) was used to observe the bonding interfaces and gap distances. TEM (Talos F200x, FEI) was also performed to confirm the atomic bonding across the Al_2O_3/SiO_2 interfaces. EDX element line scanning and mapping were conducted to study the element distributions. The FIB technique was used to inspect the reliability of the Al_2O_3/SiO_2 bonding interface and fabricate the TEM sample.

Numerical Simulation. The simulation was implemented by a FDTD method (Lumerical Inc.). The dielectric constants of Al_2O_3, Au, and H_2O were taken from Palik. Antisymmetric (symmetric) boundary conditions parallel (perpendicular) to the long axis of Au nanoantennas and perfect matching layers (PML) were applied to the unit cell to improve computational efficiency. The incident plane wave source was also polarized along the long axis of Au nanoantennas. A frequency-domain field and power monitor were used to record the reflected spectra.

Device Fabrication. The device fabrication process is shown in Figure S8. It involved electron beam lithography (EBL, Jeol 6300-FS), laser writer, standard lift-off processes, inductively coupled plasma reactive ion etching, electron-beam evaporator, and Al_2O_3/SiO_2 direct bonding. The liquid sensing chamber was fabricated on the SiO_2 layer thermally grown on the (100)-oriented Si substrate, while the Au nanoantenna arrays were formed on the (1000)-oriented Al_2O_3 substrate. First, the AZ1512 and PMMA-A5 photoresists were spin-coated on the isopropanol cleaned SiO_2 and Al_2O_3 surfaces, respectively. Since Al_2O_3 is insulating, a thin conducting polymer film ESpacer (Showa Denko Singapore) was spin-coated at 2000 rpm. After 1 min curing at 105 °C, laser writer, and EBL were used to write the patterns of the liquid chamber and nanoantenna arrays on the

AZ1512 and PMMA-A5, respectively. To reinforce the pattern structures after the development process, 115 °C heating for 1 min was performed. Then, 5 nm Ti followed by 95 and 40 nm Au were deposited on the patterned SiO_2 and Al_2O_3 surfaces to form the Au reflected chamber and nanoantenna arrays, respectively. Finally, the $O_2/NH_3/H_2O$ plasma-activated direct bonding process was conducted to obtain the device after a standard lift-off process. Note that direct bonding can only be achieved between smooth surfaces with <1 nm asperities. However, the deposited Au against the sloping chamber sidewall was always tens of nanometers higher than the bonding surfaces. It always made the bonding fail. Therefore, we adopted a two-step laser writer process to make the Au reflector grow as an isolated island in the middle of the cavity without contacting the sidewall, as shown in Figure S8a−e.

Infrared measurements. Infrared measurements were performed by a Fourier transform infrared microscope (Agilent Cary 610 Series). The resolution of the response spectra is 8 cm^{-1}. The measured area is 200 × 200 μm^2. A polarizer was used to make the polarization of the incident light along the longitudinal direction of nanoantennas. Before the device performance test, the background of reflection signals is calibrated with a bare Au mirror.

ASSOCIATED CONTENT

Supporting Information

The Supporting Information is available free of charge at https://pubs.acs.org/doi/10.1021/acsnano.0c05794.

> Supporting Notes S1−S10, including simulation results, theoretical calculations, material characterizations, and spectra tuning for the fabrication and performance test of 3D plasmonic Al_2O_3-based MIR sensing platform (PDF)
>
> Movie S1: The capillary force test for the liquid flow in the nanochannel and sensing chamber (MP4)

AUTHOR INFORMATION

Corresponding Authors

Chenxi Wang − *State Key Laboratory of Advanced Welding and Joining, Harbin Institute of Technology, Harbin 150001, China;* orcid.org/0000-0003-0576-1055; Email: wangchenxi@hit.edu.cn

Yanhong Tian − *State Key Laboratory of Advanced Welding and Joining, Harbin Institute of Technology, Harbin 150001, China;* orcid.org/0000-0002-5877-7096; Email: tianyh@hit.edu.cn

Chengkuo Lee − *Department of Electrical and Computer Engineering, Center for Intelligent Sensors and MEMS (CISM), and NUS Graduate School for Integrative Sciences and Engineering, National University of Singapore, Singapore 117576 Singapore;* orcid.org/0000-0002-8886-3649; Email: elelc@nus.edu.sg

Authors

Jikai Xu − *State Key Laboratory of Advanced Welding and Joining, Harbin Institute of Technology, Harbin 150001, China; Department of Electrical and Computer Engineering, National University of Singapore, Singapore 117576 Singapore;* orcid.org/0000-0001-8487-5522

Zhihao Ren − *Department of Electrical and Computer Engineering and Center for Intelligent Sensors and MEMS (CISM), National University of Singapore, Singapore 117576 Singapore;* orcid.org/0000-0002-2520-0784

Bowei Dong − *Department of Electrical and Computer Engineering and Center for Intelligent Sensors and MEMS (CISM), National University of Singapore, Singapore 117576 Singapore*

Xinmiao Liu − *Department of Electrical and Computer Engineering and Center for Intelligent Sensors and MEMS (CISM), National University of Singapore, Singapore 117576 Singapore*

Complete contact information is available at: https://pubs.acs.org/10.1021/acsnano.0c05794

Author Contributions

‖These authors contributed equally to this work.

Notes

The authors declare no competing financial interest.

ACKNOWLEDGMENTS

This work was supported by the National Natural Science Foundation of China (grant no. 51975151), the research grant of CRP-15th (NRF-CRP15-2015-02) at the National University of Singapore (NUS), Singapore, the Heilongjiang Provincial Natural Science Foundation of China (grant no. LH2019E041), and China Postdoctoral Science Foundation (grant no. 2017M610207). J.X. also thanks the China Scholarship Council (file no. 201906120176) for supporting this work.

REFERENCES

(1) Potyrailo, R. A. Multivariable Sensors for Ubiquitous Monitoring of Gases in the Era of Internet of Things and Industrial Internet. *Chem. Rev.* **2016**, *116*, 11877−11923.

(2) Wei, J.; Li, Y.; Chang, Y.; Hasan, D. M. N.; Dong, B.; Ma, Y.; Qiu, C.-W.; Lee, C. Ultrasensitive Transmissive Infrared Spectroscopy *via* Loss Engineering of Metallic Nanoantennas for Compact Devices. *ACS Appl. Mater. Interfaces* **2019**, *11*, 47270−47278.

(3) Dong, L.; Yang, X.; Zhang, C.; Cerjan, B.; Zhou, L.; Tseng, L. M.; Zhang, Y.; Alabastri, A.; Nordlander, P.; Halas, N. J. Nanogapped Au Antennas for Ultrasensitive Surface-Enhanced Infrared Absorption Spectroscopy. *Nano Lett.* **2017**, *17*, 5768−5774.

(4) John-Herpin, A.; Tittl, A.; Altug, H. Quantifying the Limits of Detection of Surface-Enhanced Infrared Spectroscopy with Grating Order-Coupled Nanogap Antennas. *ACS Photonics* **2018**, *5*, 4117−4124.

(5) Chang, Y.; Hasan, D.; Dong, B.; Wei, J.; Ma, Y.; Zhou, G.; Ang, K. W.; Lee, C. All-Dielectric Surface-Enhanced Infrared Absorption-Based Gas Sensor Using Guided Resonance. *ACS Appl. Mater. Interfaces* **2018**, *10*, 38272−38279.

(6) Chen, C.; Mohr, D. A.; Choi, H.-K.; Yoo, D.; Li, M.; Oh, S.-H. Waveguide-Integrated Compact Plasmonic Resonators for On-Chip Mid-Infrared Laser Spectroscopy. *Nano Lett.* **2018**, *18*, 7601−7608.

(7) Hasan, D.; Lee, C. Hybrid Metamaterial Absorber Platform for Sensing of CO_2 Gas at Mid-IR. *Adv. Sci.* **2018**, *5*, 1700581.

(8) Feng, L.; Huo, P.; Liang, Y.; Xu, T. Photonic Metamaterial Absorbers: Morphology Engineering and Interdisciplinary Applications. *Adv. Mater.* **2019**, 1903787.

(9) Hwang, I.; Yu, J.; Lee, J.; Choi, J.-H.; Choi, D.-G.; Jeon, S.; Lee, J.; Jung, J.-Y. Plasmon-Enhanced Infrared Spectroscopy Based on Metamaterial Absorbers with Dielectric Nanopedestals. *ACS Photonics* **2018**, *5*, 3492−3498.

(10) Kang, S.; Qian, Z.; Rajaram, V.; Calisgan, S. D.; Alu, A.; Rinaldi, M. Ultra-Narrowband Metamaterial Absorbers for High Spectral Resolution Infrared Spectroscopy. *Adv. Opt. Mater.* **2019**, *7*, 1801236.

(11) Zhou, H.; Yang, C.; Hu, D.; Li, D.; Hui, X.; Zhang, F.; Chen, M.; Mu, X. Terahertz Biosensing Based on Bi-Layer Metamaterial Absorbers toward Ultra-High Sensitivity and Simple Fabrication. *Appl. Phys. Lett.* **2019**, *115*, 143507.

(12) Dayal, G.; Chin, X. Y.; Soci, C.; Singh, R. High-Q Plasmonic Fano Resonance for Multiband Surface-Enhanced Infrared Absorption of Molecular Vibrational Sensing. *Adv. Opt. Mater.* **2017**, *5*, 1600559.

(13) Dong, B.; Ma, Y.; Ren, Z.; Lee, C. Recent Progress in Nanoplasmonics-Based Integrated Optical Micro/Nano-Systems. *J. Phys. D: Appl. Phys.* **2020**, *53*, 213001.

(14) Chang, Y.; Wei, J.; Lee, C. Metamaterials-From Fundamentals and MEMS Tuning Mechanisms to Applications. *Nanophotonics* **2020**, *9*, 3049−3070.

(15) Rodrigo, D.; Tittl, A.; Ait-Bouziad, N.; John-Herpin, A.; Limaj, O.; Kelly, C.; Yoo, D.; Wittenberg, N. J.; Oh, S.-H.; Lashuel, H. A.; Altug, H. Resolving Molecule-Specific Information in Dynamic Lipid Membrane Processes with Multi-Resonant Infrared Metasurfaces. *Nat. Commun.* **2018**, *9*, 2160.

(16) Hasan, D.; Pitchappa, P.; Wang, J.; Wang, T.; Yang, B.; Ho, C. P.; Lee, C. Novel CMOS-Compatible Mo-AlN-Mo Platform for Metamaterial-Based Mid-IR Absorber. *ACS Photonics* **2017**, *4*, 302−315.

(17) Brown, L. V.; Zhao, K.; King, N.; Sobhani, H.; Nordlander, P.; Halas, N. J. Surface-Enhanced Infrared Absorption Using Individual Cross Antennas Tailored to Chemical Moieties. *J. Am. Chem. Soc.* **2013**, *135*, 3688−3695.

(18) Park, H.-R.; Ahn, K. J.; Han, S.; Bahk, Y.-M.; Park, N.; Kim, D.-S. Colossal Absorption of Molecules inside Single Terahertz Nanoantennas. *Nano Lett.* **2013**, *13*, 1782−1786.

(19) Adato, R.; Yanik, A. A.; Amsden, J. J.; Kaplan, D. L.; Omenetto, F. G.; Hong, M. K.; Erramilli, S.; Altug, H. Ultra-Sensitive Vibrational Spectroscopy of Protein Monolayers with Plasmonic Nanoantenna Arrays. *Proc. Natl. Acad. Sci. U. S. A.* **2009**, *106*, 19227−19232.

(20) Shi, Q.; Dong, B.; He, T.; Sun, Z.; Zhu, J.; Zhang, Z.; Lee, C. Progress in Wearable Electronics/Photonics-Moving toward the Era of Artificial Intelligence and Internet. *InfoMater.* **2020**, DOI: 10.1002/inf2.12122

(21) Ma, Y.; Dong, B.; Lee, C. Progress of Infrared Guided-Wave Nanophotonic Sensors and Devices. *Nano Converg.* **2020**, *7*, 12.

(22) Le, T. H. H.; Tanaka, T. Plasmonics-Nanofluidics Hydrid Metamaterial: An Ultrasensitive Platform for Infrared Absorption Spectroscopy and Quantitative Measurement of Molecules. *ACS Nano* **2017**, *11*, 9780−9788.

(23) Ren, Z.; Chang, Y.; Ma, Y.; Shih, K.; Dong, B.; Lee, C. Leveraging of MEMS Technologies for Optical Metamaterials Applications. *Adv. Opt. Mater.* **2020**, *8*, 1900653.

(24) Su, D.-S.; Tsai, D. P.; Yen, T.-J.; Tanaka, T. Ultrasensitive and Selective Gas Sensor Based on a Channel Plasmonic Structure with an Enormous Hot-Spot Region. *ACS Photonics* **2019**, *4*, 2900−2907.

(25) Shih, K.; Ren, Z.; Wang, C.; Lee, C. MIR Plasmonic Liquid Sensing in Nano-Metric Space Driven by Capillary Force. *J. Phys. D: Appl. Phys.* **2019**, *52*, 394001.

(26) Adato, R.; Artar, A.; Erramilli, S.; Altug, H. Engineered Absorption Enhancement and Induced Transparency in Coupled Molecular and Plasmonic Resonator Systems. *Nano Lett.* **2013**, *13*, 2584−2591.

(27) Le, T. H. H.; Morita, A.; Mawatari, K.; Kitamori, T.; Tanaka, T. Metamaterials-Enhanced Infrared Spectroscopic Study of Nano-confined Molecules by Plasmonics-Nanofluidics Hybrid Device. *ACS Photonics* **2018**, *5*, 3179−3188.

(28) Whitesides, G. M. The Origins and the Future of Microfluidics. *Nature* **2006**, *442*, 368−373.

(29) Wu, J.; Lee, N. Y. One-Step Surface Modification for Irreversible Bonding of Various Plastics with Poly (dimethylsiloxane) Elastomer at Room Temperature. *Lab Chip* **2014**, *14*, 1564−1571.

(30) Shinohara, H.; Kasahara, T.; Shoji, S.; Mizuno, J. Studies on Low-Temperature Direct Bonding of VUV/O_3-, VUV- and O_2 Plasma-Pre-Treated Poly-Methylmethacrylate. *J. Micromech. Microeng.* **2011**, *21*, No. 085028.

(31) Xu, Y. Nanofluidics: A New Arena for Materials Science. *Adv. Mater.* **2018**, *30*, 1702419.

(32) Mawatari, K.; Kazoe, Y.; Shimizu, H.; Pihosh, Y.; Kitamori, T. Extended-Nanofluidics: Fundamental Technologies, Unique Liquid Properties, and Application in Chemical and Bio Analysis Methods and Devices. *Anal. Chem.* **2014**, *86*, 4068−4077.

(33) Xu, Y.; Wang, C.; Li, L.; Matsumoto, N.; Jang, K.; Dong, Y.; Mawatari, K.; Suga, T.; Kitamori, T. Bonding of Glass Nanofluidic Chips at Room Temperature by a One-Step Surface Activation Using O_2/CF_4 Plasma Treatment. *Lab Chip* **2013**, *13*, 1048−1052.

(34) He, R.; Yamauchi, A.; Suga, T. Sequential Plasma Activation Methods for Hydrophilic Direct Bonding at Sub-200 °C. *Jpn. J. Appl. Phys.* **2018**, *57*, No. 02BD03.

(35) Xu, J.; Wang, C.; Wang, T.; Wang, Y.; Kang, Q.; Liu, Y.; Tian, Y. Mechanisms for Low-Temperature Direct Bonding of Si/Si and Quartz/Quartz *via* VUV/O_3 Activation. *RSC Adv.* **2018**, *8*, 11528−11535.

(36) Wang, C.; Xu, J.; Qi, X.; Liu, Y.; Tian, Y.; Wang, C.; Suga, T. Direct Homo/Heterogeneous Bonding of Silicon and Glass Using Vacuum Ultraviolet Irradiation in Air. *J. Electrochem. Soc.* **2018**, *165*, H3093−H3098.

(37) Adato, R.; Altug, H. *In-Situ* Ultra-Sensitive Infrared Absorption Spectroscopy of Biomolecule Interactions in Real Time with Plasmonic Nanoantennas. *Nat. Commun.* **2013**, *4*, 2154.

(38) Le, T. H. H.; Morita, A.; Mawatari, K.; Kitamori, T.; Tanaka, T. Metamaterials-Enhanced Infrared Spectroscopic Study of Nano-confined Molecules by Plasmonics-Nanofluidics Hybrid Device. *ACS Photonics* **2018**, *5*, 3179−3188.

(39) Limaj, O.; Etezadi, D.; Wittenberg, N. J.; Rodrigo, D.; Yoo, D.; Oh, S.-H.; Altug, H. Infrared Plasmonic Biosensor for Real-Time and Label-Free Monitoring of Liquid Membranes. *Nano Lett.* **2016**, *16*, 1502−1508.

(40) Dong, B.; Luo, X.; Zhu, S.; Li, M.; Hasan, D.; Zhang, L.; Chua, S. J.; Wei, J.; Chang, Y.; Lo, G.-Q.; Ang, K. W.; Kwong, D.-L.; Lee, C. Aluminum Nitride on Insulator (AlNOI) Platform for Mid-Infrared Photonics. *Opt. Lett.* **2019**, *44*, 73−76.

(41) Leitis, A.; Heßler, A.; Wahl, S.; Wuttig, M.; Taubner, T.; Tittl, A.; Altug, H. All-Dielectric Programmable Huygens' Metasurfaces. *Adv. Funct. Mater.* **2020**, *30*, 1910259.

(42) Wei, J.; Lee, C. Anomalous Plasmon Hybridization in Nanoantennas near Interfaces. *Opt. Lett.* **2019**, *44*, 6041−6044.

(43) Leitis, A.; Tittl, A.; Liu, M.; Lee, B. H.; Gu, M. B.; Kivshar, Y. S.; Altug, H. Angle-Multiplexed All-Dielectric Metasurfaces for Broadband Molecular Fingerprint Retrieval. *Sci. Adv.* **2019**, *5*, eaaw2871.

(44) Tittl, A.; Leitis, A.; Liu, M.; Yesilkoy, F.; Choi, D.-Y.; Neshev, D. N.; Kivshar, Y. S.; Altug, H. Imaging-Based Molecular Barcoding with Pixelated Dielectric Metasurfaces. *Science* **2018**, *360*, 1105−1109.

(45) Haus, H. A. *Waves and Fields in Optoelectrics*; Prentice-Hall, Inc.: Englewood Cliffs, NJ, 1984.

(46) Wang, C.; Wang, Y.; Tian, Y.; Wang, C.; Suga, T. Room-Temperature Direct Bonding of Silicon and Quartz Glass Wafers. *Appl. Phys. Lett.* **2017**, *110*, 221602.

(47) Wang, C.; Liu, Y.; Li, Y.; Tian, Y.; Wang, C.; Suga, T. Mechanisms for Room-Temperature Fluorine Containing Plasma Activated Bonding. *ECS J. Solid State Sci. Technol.* **2017**, *6*, P373−P378.

(48) Wang, C.; Liu, Y.; Suga, T. A Comparative Study: Void Formation in Silicon Wafer Direct Bonding by Oxygen Plasma Activation with and without Fluorine. *ECS J. Solid State Sci. Technol.* **2017**, *6*, P7−P13.

(49) Xu, J.; Wang, C.; Tian, Y.; Wu, B.; Wang, S.; Zhang, H. Glass-on-$LiNbO_3$ Heterostructure Formed *via* a Two-Step Plasma Activated Low-Temperature Direct Bonding Method. *Appl. Surf. Sci.* **2018**, *459*, 621−629.

(50) Xu, J.; Wang, C.; Ji, X.; An, Q.; Tian, Y.; Suga, T. Direct Bonding of High Dielectric Oxides for High-Performance Transistor Applications. *Scr. Mater.* **2020**, *178*, 307−312.

(51) Howlader, M. M. R.; Kagami, G.; Lee, S. H.; Wang, J.; Kim, M. J.; Yamauchi, A. Sequential Plasma-Activated Bonding Mechanism of Silicon/Silicon Wafers. *J. Microelectromech. Syst.* **2010**, *19*, 840−848.

(52) Xu, J.; Wang, C.; Wang, T.; Liu, Y.; Tian, Y. Direct Bonding of Silicon and Quartz Glass Using VUV/O_3 Activation and a Multistep Low-Temperature Annealing Process. *Appl. Surf. Sci.* **2018**, *453*, 416−422.

(53) Mu, F.; He, R.; Suga, T. Room Temperature GaN-Diamond Bonding for High-Power GaN-on-Diamond Devices. *Scr. Mater.* **2018**, *150*, 148−151.

(54) Xu, J.; Wang, C.; Zhang, R.; Cheng, J.; Li, G.; Xiang, J.; Tian, Y. VUV/O_3 Activated Direct Heterogeneous Bonding towards High-Performance $LiNbO_3$-Based Optical Devices. *Appl. Surf. Sci.* **2019**, *495*, 143576.

(55) Xu, Y.; Wang, C.; Dong, Y.; Li, L.; Jang, K.; Mawatari, K.; Suga, T.; Kitamori, T. Low-Temperature Direct Bonding of Glass Nanofluidic Chips Using a Two-Step Plasma Surface Activation Process. *Anal. Bioanal. Chem.* **2012**, *402*, 1011−1018.

(56) Shin, J.; Shen, J.-T.; Fan, S. Three-Dimensional Metamaterials with an Ultrahigh Effective Refractive Index over a Broad Bandwidth. *Phys. Rev. Lett.* **2009**, *102*, No. 093903.

(57) Liu, N.; Mesch, M.; Weiss, T.; Hentschel, M.; Giessen, H. Infrared Perfect Absorber and Its Application as Plasmonic Sensor. *Nano Lett.* **2010**, *10*, 2342−2348.

(58) Peters, C.; Thien, J.; Wolff, L.; Koß, H.-J.; Bardow, A. Quaternary Diffusion Coefficients in Liquids from Microfluidics and Raman Microspectroscopy: Cyclohexane + Toluene + Acetone + Methanol. *J. Chem. Eng. Data* **2020**, *65*, 1273−1288.

(59) Zhu, Q.; D'Agostino, C.; Ainte, M.; Mantle, M. D.; Gladden, L. F.; Ortona, O.; Paduano, L.; Ciccarelli, D.; Moggridge, G. D. Prediction of Mutual Diffusion Coefficients in Binary Liquid Systems with One Self-Associating Component From Viscosity Data and Intradiffusion Coefficients at Infinite Dilution. *Chem. Eng. Sci.* **2016**, *147*, 118−127.

(60) Chan, T. C.; Tang, W. Y.; Chang, N. W.; Chan, C. H. C. Diffusion of Aromatic Isomers in Acetone: An Investigation on the Effects of Intramolecular and Intermolecular Hydrogen Bonding. *J. Phys. Chem. B* **2017**, *121*, 10882−10892.

(61) Moggridge, G. Prediction of the Mutual Diffusivity in Binary Non-Ideal Liquid Mixtures from the Tracer Diffusion Coefficients. *Chem. Eng. Sci.* **2012**, *71*, 226−238.

(62) Nugroho, F. A. A.; Albinsson, D.; Antosiewicz, T. J.; Langhammer, C. Plasmonic Metasurface for Spatially Resolved Optical Sensing in Three Dimensions. *ACS Nano* **2020**, *14*, 2345−2353.

(63) Chang, Y.; Dong, B.; Ma, Y.; Wei, J.; Ren, Z.; Lee, C. Vernier Effect-Based Tunable Mid-Infrared Sensor Using Silicon-On-Insulator Cascaded Rings. *Opt. Express* **2020**, *28*, 6251−6260.

(64) Offermans, P.; Schaafsma, M. C.; Rodriguez, S. R. K.; Zhang, Y.; Crego-Calama, M.; Brongersma, S. H.; Gomez Rivas, J. Universal Scaling of the Figure of Merit of Plasmonic Sensors. *ACS Nano* **2011**, *5*, 5151−5157.

(65) Janzen, T.; Zhang, S.; Mialdun, A.; Guevara-Carrion, G.; Vrabec, J.; He, M.; Shevtsova, V. Mutual Diffusion Governed by Kinetics and Thermodynamics in the Partially Miscible Mixture Methanol + Cyclohexane. *Phys. Chem. Chem. Phys.* **2017**, *19*, 31856−31873.

(66) Winkelmann, J. In *Diffusion in Gases, Liquids and Electrolytes. Nonelectrolyte Liquids and Liquid Mixtures - Part 2: Liquid Mixtures*; Lechner, M. D., Ed.; Springer-Verlag: Berlin, Heidelberg, 2017.

(67) Cussler, E. L. *Diffusion: Mass Transfer in Fluid Systems*; Cambridge University Press: Cambridge, UK, 2007.

(68) Shiotari, A.; Sugimoto, Y. Ultrahigh-Resolution Imaging of Water Networks by Atomic Force Microscopy. *Nat. Commun.* **2017**, *8*, 14313.

(69) Verdaguer, A.; Sacha, G. M.; Bluhm, H.; Salmeron, M. Molecular Structure of Water at Interfaces: Wetting at the Nanometer Scale. *Chem. Rev.* **2006**, *106*, 1478−1510.

(70) Chan, T. C.; Chan, C. H. C.; Tang, W. Y.; Chang, N. W. Effects of Hydrogen Bonding on Diffusion of Aromatic Compounds in Acetone: An Experimental Investigation from 268.2 to 328.2 K. *J. Phys. Chem. B* **2018**, *122*, 9236−9249.

(71) Shih, K.; Pitchappa, P.; Jin, L.; Chen, C.-H.; Singh, R.; Lee, C. Nanofluidic Terahertz Metasensor for Sensing in Aqueous Environment. *Appl. Phys. Lett.* **2018**, *113*, No. 071105.